Improved activity and stability of chlorobenzene oxidation over transition metal-substituted spinel-type catalysts supported on cordierite

Article

Accepted Version

Improved activity and stability of chlorobenzene oxidation over transition metal-substituted spinel-type catalysts supported on cordierite

Qiong Huang[1, *], Gongda Xu[1], Kaiqing Zhang[2], Jie Zhu[1], Han Si[1], Bo Yang[1], Tao Tao[1], Yunxia Zhao[1], Mindong Chen[1] and Hong Yang[1, 3, *]

[1] Jiangsu Collaborative Innovation Center of Atmospheric Environment and Equipment Technologies, Jiangsu Key Laboratory of Atmospheric Environmental Monitoring & Pollution Control, School of Environmental Science & Engineering, Nanjing University of Information Science & Technology, Nanjing 210044, China;

[2] Reading Academy, Nanjing University of Information Science & Technology, Nanjing 210044, China;

[3] Department of Geography and Environmental Science, University of Reading, Whiteknights, Reading, RG6 6AB, UK

*Corresponding author 1: Dr. Qiong Huang

School of Environmental Science and Engineering, Nanjing University of Information Science & Technology, Nanjing 210044, China

Address: No. 219 Ningliu Road, Nanjing University of Information Science & Technology, School of Environmental Science and Engineering, 210044, Nanjing, China

E–mail: hqhaixia@163.com (Q.H.)

Tel: +86 25 58731090 Fax: +86 25 58731090

*Corresponding author 2: Dr. Hong Yang

Department of Geography and Environmental Science, University of Reading, Whiteknights, Reading, RG6 6AB, UK

E–mail: hongyanghy@gmail.com (H. Y.)

Tel: +44 (0)1183787750

ABSTRACT: Industrial catalysts usually encounter great challenges in Cl· deactivation, toxic by-products generation, and stability with a long running operation for catalytic oxidation of chlorinated volatile organic compounds (CVOCs). In this research, spinel-type oxides with transition metal substituted as active oxides supported on cordierite (Crd) was identified to catalytic degradation of chlorobenzene (CB). The $Cu_{1.4}Mn_{1.6}O_4$ spinel-type oxides considered as the main active oxides have been identified, which were confirmed by XRD and TEM. The activities of these $CuM_xMn_{2-x}O_4$ catalysts were markedly improved by lower calcining temperature and shorter time. $CuCe_{0.25}Mn_{1.75}O_4$/Crd catalyst displayed the highest activity and good stability due to that CeO_2 nano-rods structure conducive to increase the O_{ads} amount, the dispersion of active oxides, the strength of weak acidity, the surface areas and pore volume. Moreover, spinel-type with CeO_2 doping exhibited high performance in CVOCs elimination attributed to the high storage capacity of oxygen, plentiful oxygen vacancies, good efficiency in breaking C-Cl bond and the easy shuttles between Ce^{3+} and Ce^{4+}, which were demonstrated by XPS. The results indicate that CeO_2, O_{ads}, and ·OH have beneficial effects on the removing Cl· into benzene, and then improving the ring-opening of CB for CB degradation.

Keywords: CVOCs; Catalytic degradation; Spinel-type oxides; Cordierite; Transition metal substitution

1. Introduction

1,2-dichloroethane (DCE), trichloroethylene (TCE), dichloromethane (DCM), chlorobenzene (CB), etc. are important members of CVOCs, which are extensively applied in industry as raw materials or solvents [1, 2]. In the last decades, CVOCs have received increasing attention due to the damage of these compounds as important atmospheric pollutants to the ecological environment, flora and fauna, and human health [3]. Owing to the permanent large toxicity and difficulty in degradation, effective technologies are needed to reduce CVOCs emission [4]. Among the methods of CVOCs elimination, catalytic oxidation has emerged as a promising method to degrade CVOCs into relatively less harm gases, for example, CO_2, H_2O and HCl, attributed to the low energy consumption and the high oxidation efficiency and [5, 6]. However, the catalytic oxidation has also been constrained by activity, stability, and poisoning [3]. In order to improve the activity of CVOCs elimination, some studies have been conducted for three typical catalysts: noble metal, transition metal oxides and zeolites [7, 8, 9].

Noble metals, for example, Pt and Pd, have been identified as high activity and effective material for the elimination of VOCs and CVOCs [10]. However, due to the high price of precious metals, the $Cl^{\bullet}$ deactivation, and the formation of polychlorinated compounds as by-products are severely limited in industry [11]. Meanwhile, these noble metals catalysts could be synthesized with high specific surface areas in order to improve the dispersion of precious metals [12, 13].

In recent years, zeolites with abundant acid solid [2, 14, 15, 16] such as H-MOR, H-ZSM5, H-BETA, have received more attention, due to the abundant Brønsted and Lewis acid selected to improve the adsorption and oxidation performance, and resistance to Cl poisoning. Weng et al [17] indicated that the $Mn_{0.8}Ce_{0.2}O_2$ showed deactivation attributed to the accumulation of chloride or coke on the surface of Mn-Ce mixed oxides. While as for the $Mn_{0.8}Ce_{0.2}O_2$/HZSM-5, the process for catalytic oxidation of CB started onto the adsorption of Brønsted acid sites at first, where CB was broke down into phenolates, benzoquinone or cyclohexanone species. Therefore, to some extent, these Cl or coke could be partially caught by HZSM-5 to defend these active sites. Therefore, the $Mn_{0.8}Ce_{0.2}O_2$/HZSM-5 exhibited the highest activity and stability for 50h and the T_{90} was 250 °C with a WHSV at 15 000 mL/g in the humid aging condition. Wang et al [18] prepared a series of Pt_xRu_y/ HZSM-5 catalysts with different Pt/Ru ratios by an improved co-impregnation method and the results indicated that Pt and Ru nano-particles were highly dispersed on hierarchical HZSM-5 supports in form of Pt–O–Ru structures, which improves the reducibility and acidity of the catalysts. The relationship of enhanced redox and acidic properties with close structure-activity for CB oxidation activity were observed.

Dai et al [2] found that CeO_2@HZSM-5 showed better resistance to the Cl poisoning and carbon deposition owing to the formed polyaromatic or non-activated coke, which could be eliminated via *in situ* oxidation by these active oxygen species. The naked HZSM-5 with acid sites can tolerate for the direct adsorption of chlorination and protect CeO_2. However, zeolites catalysts are also constrained by two problems: less activity at low temperature [1], and more byproducts of polychlorinated hydrocarbons [6].

Therefore, much effort has focused on these catalysts synthesized by transition metal oxides, like V_2O_5, Cr_2O_3, Co_3O_4, MnO_2, and NiO, by resisting the deactivation to a larger extent [19, 20, 21, 22]. However, for some catalysts with one of transition metal oxide, the formation of volatile species at low temperature, such as metal chloride or metal chloride oxide, and even the loss of active sites adsorbing HCl/Cl_2 may lead to partial deactivation, which will constrain its applications in industry [23]. According to the synergetic effect on the interactions of metal oxides-metal oxides or metal oxides-support, composite or mixed metal oxides can enhance the surface acidic sites and significantly promote the mobility of the active oxygen on the surface of catalysts [21]. Studies found composite oxides [1, 24, 25], such as perovskite-type and spinel, and mixed oxides, for example, MnO_x/CeO_2[26, 27], VO_x/CeO_2 [28], $SnO_x–MnO_x–TiO_2$ [29], CeO_2/TiO_2 [30], Cr/TiO_2 [31], and others [32], can be replaced by transition metal oxides, according to the lowering of cost, high oxidation activity and thermal stability for CVOCs degradation. According to reports, CeO_2 show a high performance in eliminating CVOCs due to the significant effect in breaking the C-Cl bond [33, 34]. But, it is still easy to be inactivated owing to these large amount of $Cl^{\bullet}$ adsorption on the active sites of CeO_2.

As the third catalysts of transition metal oxides have received more attention owing to the high activity and good tolerance to Cl poisoning [29, 35]. In these transition metal oxides, ceria-based oxides, like CeO_2-TiO_2 [6], CeO_2-FeO_x [5], CeO_2-CrO_x [33, 36], CeO_2-VO_x [28, 37], CeO_2-WO_x [3], and CeO_2-MnO_x [14, 26, 38], have attracted more attention due to the high oxygen storage capacity, Ce^{4+}/Ce^{3+} redox properties of cerium oxide, and the strong interplay between MO_x and CeO_2. Recently, composite oxides as perovskite-type and spinel-type were also identified as feasible catalysts to complete catalytic oxidation of CVOCs ascribed to good thermal stability, good tolerance to chlorine poisoning, high oxygen mobility and relatively higher activities [39]. The perovskite-type oxides, such as $LaCoO_3$ [4] and $LaMnO_3$ [40], are the commonest compounds for CVOCs oxidation. In order to further enhance the activities, it is necessary to modify these perovskite-type oxides with other transition metals, especially in the B-site. Zhang et al [41] prepared $LaMnO_3$ with the substitution of B-site, such as Ni, Co, and Fe, for vinyl chloride degradation. The result showed that the activity of $LaMnO_3$ catalysts was significantly impacted by the large amount of adsorbed oxygen species or vacancies and the low-temperature reducibility of the B-site. Higher vinyl chloride degradation could be completed due to B-site substitution, which was related to the large amount of adsorbed oxygen on the surface, the higher oxygen mobility, and the lower reducibility temperature. The catalyst ranking in terms of O_{ads} quantity from the highest to the lowest is LNMO>LCMO>LFMO>LMO. So the $LaNi_{0.2}Mn_{0.8}O_3$ displayed the best performance (T_{90}=210°C) for abatement of 1000ppm of VC in air at a GHSV of 15000h^{-1}. Moreover, $LaMnO_3$ can display a preferable performance accompanied by the good stability and durability owing to perovskite-type oxides supported by Al_2O_3, CeO_2, and TiO_2 [7].

However, so far, spinel-type oxides are rarely studied in depth for catalytic oxidation of CVOCs and the oxidation mechanism has not been explained, clearly. Mn-modified

Co_3O_4 ($CoCo_2O_4$) as spinel-type oxides synthesized by co-precipitation had been applied in 1, 2-dichlorobenzene oxidation [42]. The results showed that the substitute of Mn for Co^{3+} at octahedral sites can increase the concentration of Co^{2+} in the Co_3O_4 spinel-type, which involved the binding energy of lattice oxygen (O^{2-}). Although the mobility of surface-active oxygen is affected significantly by Mn doping, the catalytic activity of $Mn_xCo_{3-x}O_4$ increases with the Co^{2+} concentration enhances. The results revealed that the catalyst with Co/Mn ratio of nine presented the highest activity with T_{90} of 347 °C and high stability at least 35 h at 3000 ppm *o*-DCB and 10% O2 at GHSV = 15,000 h−1. The above-mentioned results of transition metal oxides, especially composite oxides, confirm that the performance of oxidation-reduction and the structure are important for catalytic oxidation of CVOCs. In addition, four important aspects should be considered: the performance of spinel-type oxides supported over the carrier, the Cr, Co, Fe, and others modified for spinel-type oxides, the surface acidity, and the stability. In general, powder catalyst was difficult to be widely used in industry due to secondary pollution of dust and loss of active components. Therefore, in this work, various transition metal (M= Cr, Co, Fe, Ni, and Ce) substituted the B position of spinel oxides supported on Crd as the most widely used carrier for industrial catalyst were prepared. The effects of the content of this transition or rare earth metal oxides, the molar ratio of M/Mn, surface acidity, calcining temperature and time, and stability on the properties of catalytic oxidation of CB were investigated.

2. Experiments

2.1. Catalyst preparation

Spinel-type catalysts with Cr, Co, Fe, Ni and Ce substitution supported on Crd were synthesized by the complex method with citric acid. The definite means are as follows: weigh appropriate amount of $Cu(NO_3)_2{\cdot}3H_2O$ and $Mn(NO_3)_2$ (50.0 wt%) with the Cu/Mn molar ratio at 1:2, and then add to 40ml deionized water with continuous stirring. Then a certain amount of citric acid (1/6 times of total metal ions) and another nitrate (the M/Mn molar ratio was at 1/3), such as $Fe(NO_3)_3{\cdot}9H_2O$, $Cu(NO_3)_2{\cdot}3H_2O$, $Cr(NO_3)_3{\cdot}9H_2O$, $Ni(NO_3)_2{\cdot}6H_2O$, and $Ce(NO_3)_3{\cdot}6H_2O$, were all added into the solution until completely dissolved. After stirring for 0.5 h, the above solution was heated to 80°C until the sol formed. After that, Crd were impregnated into the sol with continuous stirring for 4h and then take out with a medicine spoon. Finally, the resulting supported catalysts were dried at 80°C for 6 h and calcined at 450°C for 7 h with 30 wt% metal oxides loading. For contrast, the other catalysts with different M/Mn molar ratio, calcining temperature and time were synthesized with the same method.

2.2. Characterisation

Powder X-ray diffraction (XRD) patterns were performed on a diffractometer (D/max-RB, Shimadzu XRD-6100) with Cu K_α radiation (40 kV, 150 mA, λ = 0.15406 nm). The 2θ angle was scanned in the 2θ range of 10-80° with the scanning rate of 4°/min. N_2 static adsorption-desorption was characterized at 77 K using a Quantachrome AutosorbiQ-C apparatus. Before the testing, all samples were all pretreatment under vacuum for 4 h at 300°C. Brunauer-Emmett-Teller (BET) was used to calculate specific

surface areas (S_{BET}), while Barrett-Joyner-Halenda (BJH) was utilized to calculate average pore diameter (D_{BJH}). Scanning electron microscopy (SEM) was operated at 5.0 kV by the Hitachi S-4800 microscope to observe the surface morphologies of these samples. Meanwhile, High resolution transmission electron microscopy (HR-TEM) was conducted on a JEM-2100F operated at an acceleration voltage of 200 kV.

H_2 Temperature-programmed reduction (H_2-TPR) was performed on a TP-5080 (Xianquan, Tianjin, China) using a thermal conductivity detector (TCD) equipped with mass spectrometer (MS, INFICON IPC400 quadrupole). In each test, catalysts (50 mg) pretreated in the 5 vol.% H_2/N_2 (40 mL/min) from 30 to 450 °C and maintained at 450 °C for 1 h. After cooling down, the quartz reactor was heated to 800 °C at a rate of 15 °C/min. In the meantime, the H_2 consumption was detected by a gas chromatograph equipped with TCD, and the result was calibrated by the CuO reduction. Temperature-programmed desorption of ammonia (NH_3-TPD) was performed on the same apparatus as H_2-TPR. Typically, catalysts (100 mg) were pretreated at 550ºC under 50 mL/min N_2 for 1h and then cool down to 50ºC. Then, ammonia was absorbed by introducing a 10 vol.% NH_3/N_2 flow of 50 mL/min and kept at 50 °C until saturation state. And then, to remove the physically adsorbed ammonia, a N_2 flow 30 mL/min was injected until the stabilization of MS baseline. Finally, signal corresponding to NH_3 desorption (m/e =17) was collected by TCD from 50 to 550 °C at a rate of 10 °C/min in the He stream.

The x-ray photoelectron spectroscopy (XPS) spectra of all catalysts were recorded on a Kratos AXIS Ultra spectrometer with a monochromatized Al Kα radiation (1486.7 eV). The X-ray anode was run at 225W and the passing energy was fixed at 20 eV. C1s of adventitious carbon with at 284.6 eV was used as the reference for binding energy. The infrared spectra (IR, MAGNA-IR750) were scanned at a rate of 32 times/seconds from 4000 to 400 cm^{-1} to identify these by-products in CB degradation.

2.3. Activity measurements

Catalytic degradation of CB was performed in a continuous-flow fixed-bed reactor, which includes a quartz tube with a diameter of 8 mm and filled with the 3.0 g of synthesized catalysts (4.8 ml in volume, 5~12 mesh) in the quartz tube. The CB contained gas was generated by bubbles form with air through a self-made reactor, and then further diluted with air to maintain the CB concentration at 500ppm. And the air flow was controlled by mass flow controllers to keep the feeding flow rate at 800 mL/min and the gas space velocity (GHSV) at 15000 h^{-1}. In each experiment, The CB in outlet gas was analyzed online gas chromatography (Fuli, GC9790II) equipped with a flame ionization detector (FID) with the using of a stainless steel chromatographic column (Restek Rtx-1, 0.25 μm×0.25 μm×30 m). Besides, the reaction temperature was raised to 300 °C at first with the stabilization CB concentration for 10 min, and then heat up to 500 °C by a second temperature ramp of 10 °C/min. And these conversions calculated by the difference CB concentration were repeated three times for each time and the averages were calculated.

3. Results and discussion

3.1. X-ray powder diffraction and BET surface area measurements

The XRD spectra of spinel-type oxides are displayed in Fig. 1. Obvious characteristic diffraction peaks of Crd at 2θ = 10.4º, 21.7 º, 26.4 º, 28.4 º, 29.5 º, and 54.2 º (PDF # 12-0303) appeared on all the catalysts studied (Fig. 4(A)) [43]. However, the intensity of diffraction peaks of Crd decreased with these spinel oxides supporting ascribed to the covering of metal oxides on the surface of Crd. In the meantime, the catalysts also reveal some small diffraction peaks at 30.4 º, 35.8 º, 57.6 º, and 63.3 º, which are attributed to the $Cu_{1.4}Mn_{1.6}O_4$ spinel-type oxides [44]. Based on the above results, we can see that the Cu/Mn molar ratio was not 1:2, probably due to some of the manganese oxides exited, independently. To investigate the influence of calcining temperature and time on the crystal structure of these catalysts, the wide-angle XRD patterns of spinel catalysts with Cr, Fe and Ce substitution are detected and shown in Fig. 1(B). The support still displayed as Crd crystal, implying that high calcining temperature at 550ºC did not change the structure of Crd. Regarding spinel catalysts with CrO_x and FeO_x substitution, the characteristic peaks for $Cu_{1.4}Mn_{1.6}O_4$ spinel-type oxides could be also found in these catalysts. In the meantime, the intensity of $Cu_{1.4}Mn_{1.6}O_4$ spinel-type oxides increased with calcining temperature increasing, but the oxidation activity of these two kinds of catalysts decreased. However, for $CuCe_{0.25}Mn_{1.75}O_4$ catalysts, these oxides supported on Crd did not exhibited significant characteristic diffraction peaks for these oxides, such as MnO_x, CeO_2 or $Cu_{1.4}Mn_{1.6}O_4$, indicating that these oxides with spinel structure might be highly distributed on the surface of Crd. Therefore, $CuCe_xMn_{2-x}O_4$ catalysts exhibited higher surface areas and pore volume than other catalysts.

Fig. 1

The BET surface areas, pore volume and diameter of spinel catalysts with different M/Mn molar ratio (M=Cr, Fe, and Ce) are exhibited in Table 1. The pore-size distribution curves and N_2 adsorption/desorption isotherms are also showed in Fig. 2. The BET surface areas and pore volume of $CuCe_xMn_{2-x}O_4$/Crd were markedly larger than spinel oxides with Cr and Fe substitution. $CuCe_xMn_{2-x}O_4$/Crd with more active sites exhibited higher oxidation activity and better stability than the other catalysts. Moreover, the pore volume and BET surface areas of $CuCe_xMn_{2-x}O_4$/Crd firstly enhanced and then decreased with the CeO_2 increasing, but the corresponding activity for CB oxidation was different from the change rule of BET surface areas. Among of them, the $CuCe_{0.5}Mn_{1.5}O_4$/Crd showed the largest surface areas, but the activity was lower than $CuCe_{0.25}Mn_{1.75}O_4$/Crd, implying that the BET surface area was not the only factor to change the activity for these catalysts [3]. Fig. 5 clearly shows that these catalysts demonstrated a Type III isotherm, indicating that these catalysts display typical mesoporous materials. The hysteresis loop with a relative pressure (P/P_0) from 0.45 to 0.9 showed the existence of irregular mesopores. However, the average pore sizes (13.7 nm, 19.4 nm and 17.8nm) of $CuCe_xMn_{2-x}O_4$/Crd catalysts enhanced first and then decreased with the increasing of CeO_2. In addition, these catalysts with CeO_2 doping exhibited more macroporous structure than other samples, owing to the accumulation of CeO_2 primary nanoparticles with a large atomic diameter on the surface.

Table 1

Fig. 2

3.2 SEM and TEM characterization

Scanning electron micrographs of $CuM_xMn_{2-x}O_4$/Crd (M=Cr, Fe, and Ce) catalysts are illustrated in Fig. 3. They exhibited different morphological structures and distribution of active oxides on the surface. It was especially noticed that the high activity was closely interrelated with the distribution of these active oxides. The catalysts displayed a high dispersion of active oxides that could demonstrate higher activity for CB oxidation. $CuCrMnO_4$/Crd catalysts (Fig. 3(B)) showed a lot of irregular spherical oxides, which was beneficial to improve the activity for CB degradation, while the agglomeration effect on compaction and sintering also appeared in the sample of $CuCrMnO_4$/Crd (Fig. 3(A)). The same result occurred in the samples of $CuFe_xMn_{2-x}O_4$/Crd and $CuCe_xMn_{2-x}O_4$/Crd. As displayed in Fig. 3(E), it was excellent to find some of the nano-rods as CeO_2 on the surface of $CuCe_{0.25}Mn_{1.75}O_4$/Crd catalyst [45], which was consistent with TEM. However, it was difficult to find these CeO_2 nano-rods in the sample of $CuCeMnO_4$/Crd.

Fig. 3

Fig. 4 shows HRTEM images of $CuM_xMn_{2-x}O_4$/Crd (M=Cr, Fe, and Ce) catalysts. The interplanar spacing of 0.251nm and 0.439 nm corresponded to (3 1 1) and (1 0 0) crystal planes of $Cu_{1.4}Mn_{1.6}O_4$ and MnO, which was good agreement with XRD. The size of observed $Cu_{1.4}Mn_{1.6}O_4$ and MnO particles were about in the range of 6-10nm. The result demonstrates that not all of the manganese oxides would combine with copper oxides to form spinel complex oxides, indicating that these oxides existed in the form of mixed oxides. With the presence of CrO_x and FeO_x, no evident crystal planes of CrO_x and FeO_x and changing in morphology were observed. Except for $Cu_{1.4}Mn_{1.6}O_4$ in the samples of $CuCe_{0.25}Mn_{1.75}O_4$/Crd, it can also be observed that the (2 2 2) crystal planes of CeO_{2-x} showed plentiful oxygen vacancies with a nano-rods structure, with the length at 56 nm and width at18 nm. This result displayed the strong interplay between $Cu_{1.4}Mn_{1.6}O_4$ and CeO_{2-x} with the rising oxygen transfer in the $CuCe_{0.25}Mn_{1.75}O_4$/Crd catalysts.

Fig. 4

Fig. 7

3.3 H_2-TPR and NH_3-TPD measurements

The H_2-TPR and NH_3-TPD measurements illustrated in Fig. 5 are used to investigate the reducibility within 100-800°C (Fig. 5(A)) and surface acid properties (Fig. 5(B)) of $CuM_{0.5}Mn_{1.5}O_4$/Crd (M=Cr, Co, Fe, Ni, and Ce). The profiles were similar to those observed for $Cu_{1.4}Mn_{1.6}O_4$ composite oxides where two peaks presented, the first reduction peak at low temperature and the second intense and broad multi-composite peak at high temperature [46]. Although, it was difficult to impute the each peak to concrete redox species, according to previous reports [46], the two-step reduction indicated that the two cationic components of $Cu_{1.4}Mn_{1.6}O_4$ could be restored to Cu^0 and Mn^{2+}. Therefore, it could be inferred that the peak at low temperature (197-226°C) ascribed to the Cu^{2+} reduction and the peak at high temperature (273-420°C) corresponded to the Mn^{4+} and Mn^{3+} reduction. The manganese oxide displayed two H_2 reduction peaks; and the first (273°C, 312°C, 324°C, 338°C and 359°C) and the second (278°C, 333°C, 377°C and 420°C) were attributed to the reducibility of Mn^{4+} to Mn^{3+} and Mn^{3+} to Mn^{2+} in these samples of $CuM_{0.5}Mn_{1.5}O_4$/Crd (M=Cr, Co, Fe, Ni, and Ce), respectively. The extra peak at about 580°C was probably attributed to the reduction of

Fig. 5

Ni^{3+} to Ni^{2+} [47]. The above results illustrated that the different metal oxides doping would have a far-reaching influence on the redox properties. Among these catalysts, $CuFe_{0.5}Mn_{1.5}O_4$/Crd was the most reducible. The strong interplay between FeO_x and MnO_x can improve the mobility of active oxygen species and it was conducive to further decompose these intermediate reactants and byproducts formed for CB oxidation. In terms of $CuCe_{0.5}Mn_{1.5}O_4$/Crd, the H_2 consumption was markedly lower than other catalysts with Ni and Co oxides doping, suggesting that an amount of cerium oxides hindered the reduction of MnO_x on the surface. However, ceria oxides displayed a better performance in CVOCs decomposition, attributed to the high oxygen storage capacity, plentiful oxygen vacancies, effect in breaking C-Cl bond and the easy shuttles between Ce^{3+} and Ce^{4+} [48].

Accumulating evidences have reported that acid site was a significant role in the CVOCs elimination, so the NH_3-TPD of $CuM_{0.5}Mn_{1.5}O_4$/Crd (M=Cr, Co, Fe, Ni, and Ce) catalysts are analyzed and shown in Fig. 8(B). For the $CuCr_{0.5}Mn_{1.5}O_4$/Crd, it indicated two strong NH_3 desorption peaks appeared at about 290°C and 460°C. The two peaks at low and high temperature assigned to the weak and strong acid sites, respectively [6, 36]. For other catalysts, only one of NH_3 desorption peak located at low temperature can be found, indicating that the strength of strong acidity was evidently improved according to the CrO_x doping over $CuCr_{0.5}Mn_{1.5}O_4$/Crd. Among these catalysts, the $CuM_{0.5}Mn_{1.5}O_4$/Crd with Ni and Ce oxides doping exhibited the strongest and the weakest strength of weak acidity, showing the worst and best activities for CB oxidation. The results indicate that it was a disadvantage for catalytic oxidation of CB over the $CuM_{0.5}Mn_{1.5}O_4$/Crd catalyst with a strong strength of weak acidity, while it had little effect for CB oxidation over the catalyst with the strong acidity.

3.4 XPS analysis

XPS is an efficient technique to investigate the chemical states and surface compositions of these catalysts. The corresponding spectra of Ce 3d, Cu 2p, Mn 2p and O 1s of as-prepared catalysts are illustrated in Fig. 6. The ratios of O_{latt}/O_{ads} and Ce^{3+}/Ce^{4+} are encapsulated in Table 1. According to previous studies [46, 49], Ce $3d_{5/2}$ and Ce $3d_{3/2}$ doublets were connected with four pairs of spin-orbit doublets and denoted as v and u, assigned to deconvolution into eight peaks marked as u (u, u', u'', u''') for $3d_{3/2}$ and v (v, v', v'', v''') for $3d_{5/2}$. In all peaks, six peaks denoted as v(u), v''(u'') and v'''(u''') were assigned to Ce^{4+}, whereas the other peaks of v' and u' attributed to Ce^{3+}. Based on the contribution of Ce^{3+} features to the spectrum, the ratios of Ce^{3+}/Ce^{4+} of $CuCe_xMn_{1-x}O_4$/Crd catalysts with the Ce/Mn molar ratios at 1/7, 1/3, 1 and the calcining temperature at 350 °C, 450 °C, 550 °C for 4h were 31.0%, 25.8%, 26.4%, 25.0%, 25.2% and 24.2%, respectively. The highest Ce^{3+} content created more oxygen vacancies in $CuCe_{0.25}Mn_{1.75}O_4$/Crd, probably owing to the strong interplay between Ce and Mn [50]. Simultaneously, these oxygen vacancies were identified as active centers, this is due to theses oxygen in the defective oxides devotes to be transferred and released. While accompanied by the increasing of CeO_2 doping, a large amount of cerium oxides exhibited as CeO_2 could be found. Although the Ce^{3+} content significantly increased, the Ce^{3+}/Ce^{4+} ratio decreased with the increase of CeO_2. Base on the above results, it

Fig. 6

could also be deduced that the ratio of Ce^{3+}/Ce^{4+} didn't change with calcining temperature increasing.

Regarding Cu $2p_{2/3}$, one peak, which can be ascribed to Cu^{2+} at 933.7 eV, can be found. The satellite peaks located at 941.3–943.7 eV attributed to Cu^{2+} on the account of unfilled 3d shells. As shown in Fig. 6(B), according to the peak fitting deconvolution of Cu $2p_{2/3}$, two peaks were accessed. The results revealed that the chemical state of CuO would not transform with the variation of CeO_2 doping and calcining temperature.

The binding energy of Mn $2p_{3/2}$ located at 641.5 eV was assigned to Mn^{3+} (Mn^{2+}), which was difficult to discriminate owing to the small distinction in the values of binding energy between Mn^{3+} and Mn^{2+}, whereas the Mn $2p_{3/2}$ at 642.9 eV was ascribed to Mn^{4+} [46]. As for $CuCe_{0.25}Mn_{1.75}O_4$/Crd catalysts with different Ce/Mn molar ratios, the $Mn^{4+}/(Mn^{3+}+Mn^{2+})$ ratio increased at first and then decreased, indicating the strong interplay between Mn and Ce. Meanwhile, with the calcining temperature increasing, the $Mn^{4+}/(Mn^{3+}+Mn^{2+})$ ratios dramatically increased (71.9%, 74.4%, and 96.5%) due to the oxidization of Mn^{3+} to Mn^{4+}, which was disadvantage to improve the activity for CB degradation. According to the above results, the existence of Mn^{4+} species was crucial for $Cu_{1.4}Mn_{1.6}O_4$, which might be attributable to the redox equilibrium of Mn^{3+}/Cu^{2+}. Whereas, the calcining temperature at which the spinel catalysts synthesized would have a profound impact on the extent of electron transfer between Cu and Mn.

The asymmetrical O 1s spectra could be deconvoluted as two peaks at 529.4 eV assigned to surface lattice oxygen (O_{latt}) and at binding energy of 532.4 eV ascribed to surface adsorbed oxygen (O_{ads}, O^-, O^{2-} or O_2^{2-}). According to published results [45, 51], the O_{ads}/O_{latt} ratios acquired from the XPS measurements were all less than 1, indicating that the most of oxygen recognized as lattice oxygen on the surface of these catalysts. However, for $CuCe_xMn_{1-x}O_4$/Crd catalysts with good activities at low reaction temperature for CB oxidation, the amount of O_{latt} was considerably lower than O_{ads} and the O_{latt}/O_{ads} ratios were 32.0%, 29.5%, 29.5%, 28.3%, 21.1%, and 19.9%, separately. The above results suggested that the potential important role of O_{ads} in the good oxidation at low temperatures. With the Ce increasing, the binding energy of O_{ads} transferred to low energy, illustrating the marked change of electron cloud density of O_{ads} in the electron-transfer process. Along with the increase in calcining temperature, however, the contents of O_{ads} increased and the O_{latt} decreased with a clear reduction in catalytic activities.

3.5 Catalytic degradation of CB

The performances of spinel oxides with Cr, Co, Mn, Fe, Ni, Cu, or Ce substitution supported on Crd for CB oxidation are illustrated in Fig. 7. Crd supporter didn't exhibit any activity for catalytic oxidation of CB, even the reaction temperature up to 500°C (Fig. 7(A)). When Crd was supported with spinel-type oxides, the catalysts displayed high activity for catalytic oxidation of CB, and CB can be completely decomposed with the calcination temperature of 450°C. However, T_{90} was also much higher than noble metal-based, such as Ru/TiO_2 and Pt/TiO_2 [10], Ce-Mn oxides [45], and VO_x/CeO_2

Fig. 7

catalysts [28]. In order to improve the activity over spinel catalysts, five different kinds of transition and rare earth metal oxides including CrO_x, CoO_x, FeO_x, NiO and CeO_2, substituted the B-site of spinel oxides supported on Crd were prepared. The result exhibited that the activity of CB oxidation was all improved and T_{90} decreased from 450°C to 400°C, especially for $CuCr_{0.5}Mn_{1.5}O_4$/Crd, $CuFe_{0.5}Mn_{1.5}O_4$/Crd, and $CuCe_{0.5}Mn_{1.5}O_4$/Crd catalysts. But the $CuNi_{0.5}Mn_{1.5}O_4$/Crd catalysts showed lower activity than $CuMn_2O_4$/Crd at the same reaction temperature. To study and analyze the effect of the molar ratio of M(M=Cr, Fe and Ce)/Mn on catalytic activity, the activity of $CuCr_xMn_{2-x}O_4$/Crd, $CuFe_xMn_{2-x}O_4$/Crd and $CuCe_xMn_{2-x}O_4$/Crd with x=0.25, 0.5 and 1 were illustrated in Fig. 7(B). With the increase of x value, the performance of these three kinds of catalysts was different. Compared with the other catalysts, $CuCrMnO_4$, $CuFe_{0.25}Mn_{1.75}O_4$, and $CuCe_{0.25}Mn_{1.75}O_4$ catalysts exhibited better activities for CB degradation, thus, the effects of calcining temperature and time were further investigated and the light-off curves were described in Fig. 8.

These three kinds of catalysts ($CuCrMnO_4$, $CuFe_{0.25}Mn_{1.75}O_4$, and $CuCe_{0.25}Mn_{1.75}O_4$) were all displayed increasing activity for CB degradation with the reduction of calcining temperature and time. The order of oxidation activity was 550°C, 7h < 450°C, 7h < 550°C, 4h < 350°C, 7h ≈ 450°C, 4h ≈ 350°C, 4h (Fig. 8). The results demonstrated that the activities could be significant improvement, with low calcining temperature and a short calcining time. The formation of $Cu_{1.4}Mn_{1.6}O_4$ spinel-type oxides was consistent with XRD results. T_{90} could decrease to 300°C, even a lower reaction temperature. T_{90} was also significantly lower than some other catalysts, even some noble metal-based catalysts, such as Pd/$LaBO_3$(B=Co, Mn, Fe) [20], VO_x/CeO_2 [28], Mn-Ce-O/γ-Al_2O_3 [38] , and Ce-Mn oxides catalysts [45]. These catalysts with a calcining temperature exhibited excellent activity for CB oxidation.

These three catalysts calcinated at 450°C and for 4h ($CuCrMnO_4$, $CuFe_{0.25}Mn_{1.75}O_4$, and $CuCe_{0.25}Mn_{1.75}O_4$) had the best stabilities. Fig. 9 showed that the reaction temperature at 300°C played a crucial performance with the high activities. All these catalysts displayed good stability for CB oxidation at 24h. Among them, the $CuCe_{0.25}Mn_{1.75}O_4$ catalysts demonstrated the best results of activity, stability, and anti-poisoning, while the $CuFe_{0.25}Mn_{1.75}O_4$ showed a slight decrease in activity with the increase in time.

Fig. 9

3.6 IR analysis

To analyze the effect of the CB adsorption and reaction behaviors over spinel catalysts on the different conversions of CB (T_{20}, T_{50}, and T_{90}), IR measurement was applied to check the products of the reaction (Fig.10). According to the previous findings [38, 45, 52, 53], the bands at 3427 cm^{-1} was assigned to the O-H (ν_{O-H}) stretching vibration, which were adsorbed on the catalysts surface, whereas the bands at 1619 cm^{-1} corresponded to the absorbed O-H (ν_{O-H}) bending vibration. It was worth noting that the performance of water absorption over catalysts, which was beneficial to eliminate the HCl or Cl_2 adsorbed on the surface catalysts, was maintained as the reaction temperature increasing and CB degradation. In the meantime, the bands located at 1830 and 1700 cm^{-1} were the corresponded to vibration as aldehyde-type and the bands located at 1520

Fig. 10

cm^{-1} assigned to the ring stretching of benzene. While, the bands at 2345 cm^{-1} were ascribed to the CO_2 vibration and the bands located at 2923 and 2853 cm^{-1} were originated from the methylene (-CH_2) asymmetric stretching or C-H symmetric. Base on the measurement of IR in the current study and previous studies [14], the CB oxidation routes over $CuM_xMn_{1-x}O_4$/Crd are proposed as Fig. 11. The presence or formation of H_2O accelerated CB ring-opening and exhibited positively effect on CB degradation, probably attributed to the accumulated Cl· removal from the surface active oxides, such as MnO_x or CeO_2 [54]. According to the presence of benzene in these catalysts, the degradation process of CB was originated from dechlorination and the formation of benzene at first. And then, benzene was further oxidized into CO_2 and H_2O through a series of processes with these active adsorbed oxygen or lattice oxygen. In this process, ·OH showed the characteristic bands at 1700 cm^{-1} and had a beneficial effect on the aldehyde-type forming, which were all detected over these catalysts, even at T_{20}. Therefore, it was desirable that the ·OH radical had involved in the CB oxidation, resulting in the significant increase of CO_2 over these catalysts.

4. Conclusions

The performance of catalytic oxidation of CB over $CuM_xMn_{2-x}O_4$ (M=Cr, Co, Fe, Ni, and Ce) catalysts with different activity and stability were reported in this study. The results of XRD and TEM measurements showed that the $Cu_{1.4}Mn_{1.6}O_4$ spinel-type oxides could be detected, which displayed a significant role in CB degradation. $CuCe_{0.25}Mn_{1.75}O_4$/Crd catalyst with CeO_2 nano-rods structure is conducive to improve the O_{ads} amount, the distribution of active oxides, the weak acid strength, and pore volume and surface area, so it exhibited higher activity and better stability than other catalysts. Although H_2 consumption of $CuCe_xMn_{1-x}O_4$/Crd was markedly lower than other catalysts, ceria oxides displayed a high performance in CVOCs elimination. Ceria oxides have attracted more attention, attributed to the high oxygen storage capacity, plentiful oxygen vacancy, effect in breaking C-Cl bond and the easy shuttles with Ce^{4+} and Ce^{3+}. Meanwhile, the mechanism of CB oxidation process over $CuM_xMn_{1-x}O_4$/Crd catalysts was discussed and the IR results indicated that CeO_2, O_{ads}, and ·OH played beneficial effects on the original Cl· dissociation at first, and then ring-opening to form a variety of products, such as aldehyde-type, alkane, CO_2 and so on. Overall, our results provide meaningful solutions to prepare and design spinel-type catalysts for CVOCs degradation.

Acknowledgments

The authors would like to acknowledge the Natural Science Foundation of Jiangsu Province (No. BK20170954 and BK20150890), the National Natural Science Foundation of China (No. 21501097), the Qing Lan Project of the Jiangsu Higher Education Institutions of China. As well as the projected funded by the Priority Academic Program Development of Jiangsu Higher Education Institutions (PAPD).

Funding:

The Natural Science Foundation of Jiangsu Province (No. BK20170954 and No. BK 20150890); The National Natural Science Foundation of China (Nos. 21501097).

References

[1] S.X. Chen, Y. Wang, A.P. Jia, H.H. Liu, M.F. Luo, J.Q. Lu. Appl. Surf. Sci. 307 (2014) 178–188.

[2] Q.G. Dai, W. Wang, X.Y. Wang, G.Z. Lu. Appl. Catal. B.: Environ. 203 (2017) 31–42.

[3] Y.F. Gu, T. Cai, X.H. Gao, H.Q. Xia, W. Sun, J. Zhao, Q.G. Dai, X.Y. Wang. Appl. Catal. B.: Environ. 248 (2019) 264–276.

[4] M.J. Tian, C. He, Y.K. Yu, H. Pan, L. Smith, Z.Y. Jiang, N.B. Gao, Y.F. Jian, Z.P. Hao, Q. Zhu. Appl. Catal. A.: General. 553 (2018) 1–14.

[5] W. Wang, Q. Zhu, Q.G. Dai, X.Y. Wang. Chem. Eng. J. 307 (2017) 1037–1046.

[6] Z.N. Shi, P. Yang, F. Tao, R.X. Zhou. Chem. Eng. J. 295 (2016) 99–108.

[7] C.H. Zhang, C. Wang, S. Gil, A. Boreave, L. Retailleau, Y.L. Guo, J.L. Valverde, A. Giroir-Fendler. Appl. Catal. B.: Environ. 201 (2017) 552–560.

[8] C.C. Du, S.Y. Lu, Q.L. Wang, A.G. Buekens, M.J. Ni, D.P. Debecker. Chem. Eng. J. 334 (2018) 519–544.

[9] W. Tian, X.Y. Fan, H.S. Yang, X.B. Zhang. J. Hazard. Mater. 177 (2010) 887–891.

[10] X.L. Liu, L. Chen, T.Y. Zhu, R.L. Ning. J. Hazard. Mater. 363 (2019) 90–98.

[11] N. Ye, Y. Li, Z. Yang, J. Zheng, S.F. Zuo. Appl. Catal. A.: General. 579 (2019) 44–51.

[12] S. Zhao, K.Z. Li, S. Jiang, J.H. Li. Appl. Catal. B.: Environ. 181 (2016) 236–248.

[13] X.R. Fu, Y. Liu, W.Y. Yao, Z.B. Wu. Catal. Commun. 83 (2016) 22–26.

[14] P.F. Sun, W.L. Wang, X.X. Dai, X.L. Weng, Z.B. Wu. Appl. Catal. B.: Environ. 198 (2016) 389–397.

[15] A. Aranzabal, J.A. González-Marcos, M. Romero-Sáez, J.R. González-Velasco, M. Guillemot, P. Magnoux. Appl. Catal. B.: Environ. 88 (2009) 533–541.

[16] M.J. Tian, M.D. Ma, B.T. Xu, C.W. Chen, C. He, Z.P. Hao, R. Albilali. Catal. Sci. Technol. 8 (2018) 4503–4514.

[17] X.L. Weng, P.F. Sun, Y. Long, Q.J. Meng, Z.B. Wu. Environ. Sci. Technol. 51 (2017) 8057–8066.

[18] Y. Wang, Y. Chen, L. Zhang, G. Wang, W. Deng, L.M. Guo. Micropor. Mesopor. Mat. 308 (2020) 110538-110548.

[19] M. Wu, X.Y. Wang, Q.G. Dai, D. Li. Catal. Commun. 11 (2010) 1022–1025.

[20] H.F. Li, G.Z. Lu, Q.G. Dai, Y.Q. Wang, Y. Guo, Y.L. Guo. Appl. Catal. B.: Environ.102 (2011) 475–483.

[21] Y. Wang, K.S. Liu, J. Wu, Z.M. Hu，L.M. Guo. ACS Catal. 10 (2020) 10021–10031

[22] C. He, Y.K. Yu, Q. Shen, J.S. Chen, N.L. Qiao. Appl. Surf. Sci. 297 (2014) 59–69.

[23] Z. Cheng, J.R. Li, P. Yang, S.F. Zuo. Chinese. J. Catal. 39 (2018) 849–856.

[24] Y.J. Lu, Q.G. Dai, X.Y. Wang. Catal. Commun. 54 (2014) 114–117.

[25] J.M. Giraudon, A. Elhachimi, G. Leclercq. Appl. Catal. B.: Environ. 84 (2008) 251–261.

[26] P. Zhao, C.N. Wang, F. He, S.T. Liu. RSC. Adv, 4 (2014) 45665–45672.

[27] L.Y. Wu, F. He, J.Q. Luo, S.T. Liu. RSC. Adv, 7 (2017) 26952–26959.

[28] H. Huang, Y.F. Gu, J. Zhao, X.Y. Wang. J. Catal. 326 (2015) 54–68.

[29] J.W. Li, P. Zhao, S.T. Liu. Appl. Catal. A.: General. 482 (2014) 363–369.

[30] S. Cao, H.Q. Wang, F.X. Yu, M.P. Shi, S. Chen, X.L. Weng, Y. Liu, Z.B. Wu. J. Colloid. Interf. Sci. 463 (2016) 233–241

[31] Y.M. Jiao, X. Chen, F. He, S.T. Liu. Chem. Eng. J. 372 (2019) 107–117.

[32] G.Y. Long, M.X. Chen, Y.J. Li, J.F. Ding, R.Z. Sun, Y.F. Zhou, X.Y. Huang, G.R. Han, W.R. Zhao. Chem. Eng. J. 360 (2019) 964–973.

[33] P. Yang, S.S. Yang, Z.N. Shi, Z.H. Meng, R.X. Zhou. Appl. Catal. B.: Environ. 162 (2015) 227–235.

[34] C. He, B.T. Xu, J.W. Shi, N.L. Qiao, Z.P. Hao, J.L. Zhao. Fuel. Process. Technol. 130 (2015) 179–187.

[35] Z. Zhang, J. Huang, H.Q. Xia, Q.G. Dai, Y.F. Gu, Y.J. Lao, X.Y. Wang. J. Catal. 360 (2018) 277–289.

[36] P. Yang, Z.H. Meng, S.S. Yang, Z.N. Shi, R.X. Zhou. J. Mol. Catal. A.: Chem. 393 (2014) 75–83.

[37] Q.G. Dai, L.L. Yin, S.X. Bai, W. Wang, X.Y. Wang, X.Q. Gong, G.Z. Lu. Appl. Catal. B.: Environ.182 (2016) 598–610.

[38] M. Wu, X.Y. Wang, Q.G. Dai, Y.X. Gu, D. Li. Catal. Today. 158 (2010) 336–342.

[39] X.L. Weng, Q.J. Meng, J.J. Liu, W.Y. Jiang, S. Pattisson, Z.B. Wu. Environ. Sci. Technol. 53 (2019) 884–893.

[40] C.B. He, K.L. Pan, M.B. Chang. Environ. Sci. Pollut. R. 25 (2018) 11584–11594.

[41] C.H. Zhang, C. Wang, W.C Zhan, Y.l. Guo, Y. Guo, G.Z. Lu, A. Baylet, A. Giroir-Fendler. Appl. Catal. B.: Environ. 129 (2013) 509–516.

[42] T. Cai, H. Huang, W.Deng, Q.G. Dai, W. Liu, X.Y. Wang. Appl. Catal. B.: Environ.

166-167 (2015) 393–405.

[43] W. Li, H.Q. Ye, G.G. Liu, H.C. Ji, Y.H. Zhou, K. Han. Chinese. J. Catal. 39 (2018) 946–954.

[44] E. Ríos, S. Abarca, P. Daccarett, H. Nguyen Cong, D. Martel, .F. Marco, J.R. Gancedo, J.L. Gautier. Int. J. Hydrogen. Energy. 33 (2008) 4945–4954.

[45] Y. Wang, W. Deng, Y.F. Wang, L.M. Guo, T. Ishihara. Mol. Catal. 459 (2018) 61–70.

[46] A. Elmhamdi, L. Pascual, K. Nahdi, A. Martínez-Arias. Appl. Catal. B.: Environ. 217 (2017) 1–11.

[47] Y.S. Wu, S. Shi, S.S. Yuan, T. Bai, S.T. Xing. Appl. Surf. Sci. 479 (2019) 1262–1269.

[48] P. Yang, S.S. Yang, Z.N. Shi, F. Tao, X.L. Guo, R.X. Zhou. Chem. Eng. J. 285 (2016) 544–553.

[49] C. He, Y.K. Yu, J.W. Shi, Q. Shen, J.S. Chen, H.X. Liu. Mater. Chem. Phys. 157 (2015) 87–100.

[50] A.D. Tang, L.Q. Hu, X.H. Yang, Y.R. Jia, Y. Zhang. Catal. Commun. 82 (2016) 41–45.

[51] Y. Zhou, X.Y. Liu, K. Wang, J. Li, X.L. Zhang, X. Jin, X.Y. Tang, X.H. Zhu, R.S. Zhang, X. Jiang, B.D. Liu. Results. Phys. 12 (2019) 1893–1900.

[52] Q. Huang, H. Si, S.K. Yu, J.X. Wang, T. Tao, B. Yang, Y.X. Zhao, M.D. Chen. Environ. Technol. 41 (2020), 1664-1676.

[53] B.C. Liu, C.Y. Li, Y.F. Zhang, Y. Liu, W.T. Hu, Q. Wang, L. Han, J. Zhang. Appl. Catal. B.: Environ. 111–112 (2012) 467–475.

[54] X.Y. Wang, L. Ran, Y. Dai, Y.J. Lu, Q.G. Dai. J. Colloid. Interf. Sci. 426 (2014) 324–332.

FIGURE LEGENDS

Fig. 1. XRD patterns of $CuMn_2O_4$ catalysts: (A) Cr, Fe and Ce doping, (B) $CuCrMnO_4$, $CuFe_{0.25}Mn_{1.75}O_4$ and $CuCe_{0.25}Mn_{1.75}O_4$ catalysts under different calcining temperature and time

Fig. 2. The pore-size distribution curves and N_2 adsorption/desorption isotherms of $CuM_xMn_{2-x}O_4$ (M=Cr, Fe, and Ce) catalysts

Fig. 3. SEM images of $CuM_xMn_{2-x}O_4$/Crd (M=Cr, Fe, and Ce) catalysts (A: $CuCr_{0.25}Mn_{1.75}O_4$/Crd; B: $CuCrMnO_4$/Crd; C: $CuFe_{0.25}Mn_{1.75}O_4$/Crd; D: $CuFe_{0.5}Mn_{1.5}O_4$/Crd; E: $CuCe_{0.25}Mn_{1.75}O_4$/Crd; F: $CuCeMnO_4$/Crd)

Fig. 4. TEM images of $CuM_xMn_{2-x}O_4$/Crd (M=Cr, Fe, and Ce) catalysts (A:

$CuCrMnO_4$/Crd; B: $CuFe_{0.25}Mn_{1.75}O_4$/Crd; C and D: $CuCe_{0.25}Mn_{1.75}O_4$/Crd)

Fig. 5. The profiles of $CuM_{0.5}Mn_{1.5}O_4$/Crd (M=Cr, Co, Fe, Ni, and Ce) catalysts (A) H_2-TPR, and (B) NH_3-TPD

Fig. 6. (A) Ce 3d, (B) Cu 2p, (C) Mn 2p, (D) O 1s XPS spectra of $CuCe_xMn_{1-x}O_4$/Crd catalysts with different of Ce/Mn molar ratios and calcining temperature

Fig. 7. Catalytic oxidation of CB over $CuMn_2O_4$ catalysts: (A) Cr, Co, Mn, Fe, Ni, Cu and Ce doping; (B) $CuCr_xMn_{2-x}O_4$/Crd, $CuFe_xMn_{2-x}O_4$/Crd and $CuCe_xMn_{2-x}O_4$/Crd with x=0.25, 0.5 and 1.

Fig. 8. Catalytic oxidation of CB over (A): $CuCrMnO_4$, (B): $CuFe_{0.25}Mn_{1.75}O_4$, and (C): $CuCe_{0.25}Mn_{1.75}O_4$ catalysts under different calcining temperature and time

Fig. 9. The stabilities of $CuCrMnO_4$, $CuFe_{0.25}Mn_{1.75}O_4$, and $CuCe_{0.25}Mn_{1.75}O_4$ catalysts calcinated at 450^{o}C and for 4h for CB oxidation

Fig. 10. IR profiles of $CuM_xMn_{1-x}O_4$/Crd catalysts with the different conversion of CB (T_{20}, T_{50} and T_{90})

Fig. 11. CB oxidation routes over $CuM_xMn_{1-x}O_4$/Crd

Table Captions and Footnotes

Table 1

The structure and physical parameters of $CuM_xMn_{2-x}O_4$ (M=Cr, Fe, and Ce) catalysts with different M/Mn molar ratios

Samples	S_{BET} (m^2/g)	Pore volume (cm^3/g)	Average pore size (nm)	Ce^{3+}/Ce^{4+} (%)	$Mn^{4+}/(Mn^{3+}+Mn^{2+})$ (%)	O_{latt}/O_{ads} (%)
$CuCr_{0.25}Mn_{1.75}O_4$/Crd	12.4	0.055	16.8	-	-	-
$CuCr_{0.5}Mn_{1.5}O_4$/Crd	13.7	0.055	13.3	-	-	-
$CuCrMnO_4$/Crd	13.5	0.038	13.9	-	-	-
$CuFe_{0.25}Mn_{1.75}O_4$/Crd	13.9	0.054	11.8	-	-	-
$CuFe_{0.5}Mn_{1.5}O_4$/Crd	13.5	0.057	14.5	-	-	-
$CuFeMnO_4$/Crd	16.7	0.045	8.42	-	-	-
$CuCe_{0.25}Mn_{1.75}O_4$/Crd	21.1	0.106	13.7	31.0	72.6	32.0
$CuCe_{0.5}Mn_{1.5}O_4$/Crd	50.8	0.326	19.4	25.8	74.6	29.5
$CuCenO_4$/Crd	29.9	0.163	17.8	26.4	69.2	29.5

Fig. 1

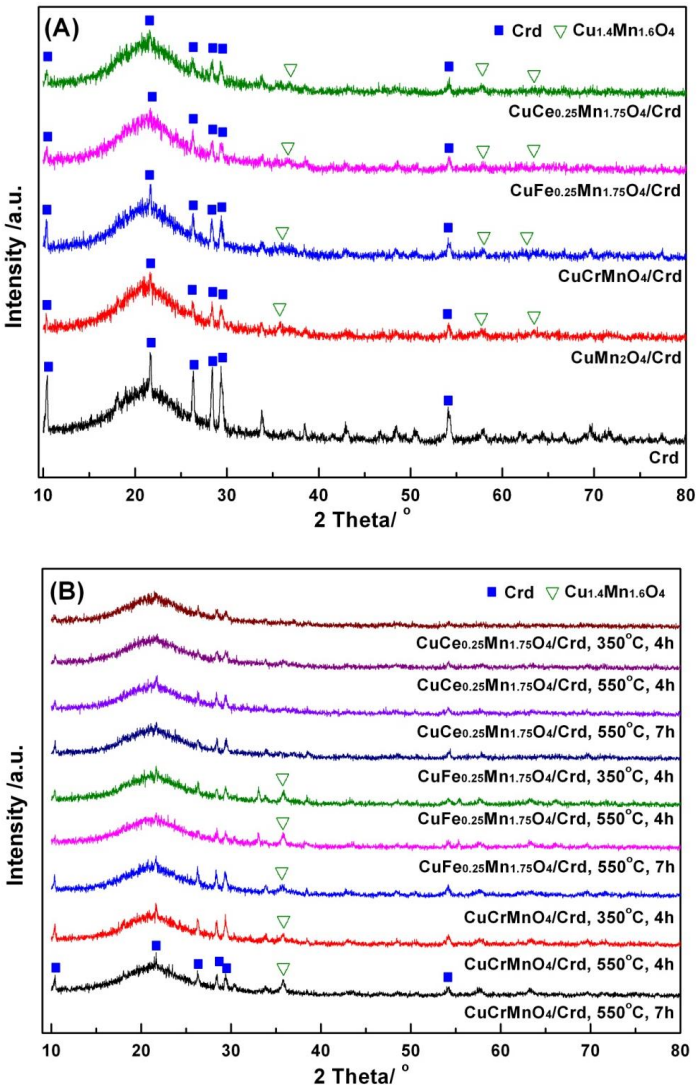
(A)
Crd
Cu1.4Mn1.6O4
CuCe0.25Mn1.75O4/Crd
CuFe0.25Mn1.75O4/Crd
CuCrMnO4/Crd
CuMn2O4/Crd
Crd
Intensity /a.u.
10
20
30
40
50
60
70
80
2 Theta/ °
(B)
Crd
Cu1.4Mn1.6O4
CuCe0.25Mn1.75O4/Crd, 350°C, 4h
CuCe0.25Mn1.75O4/Crd, 550°C, 4h
CuCe0.25Mn1.75O4/Crd, 550°C, 7h
CuFe0.25Mn1.75O4/Crd, 350°C, 4h
CuFe0.25Mn1.75O4/Crd, 550°C, 4h
CuFe0.25Mn1.75O4/Crd, 550°C, 7h
CuCrMnO4/Crd, 350°C, 4h
CuCrMnO4/Crd, 550°C, 4h
CuCrMnO4/Crd, 550°C, 7h
Intensity /a.u.
10
20
30
40
50
60
70
80
2 Theta/ °

Fig. 2

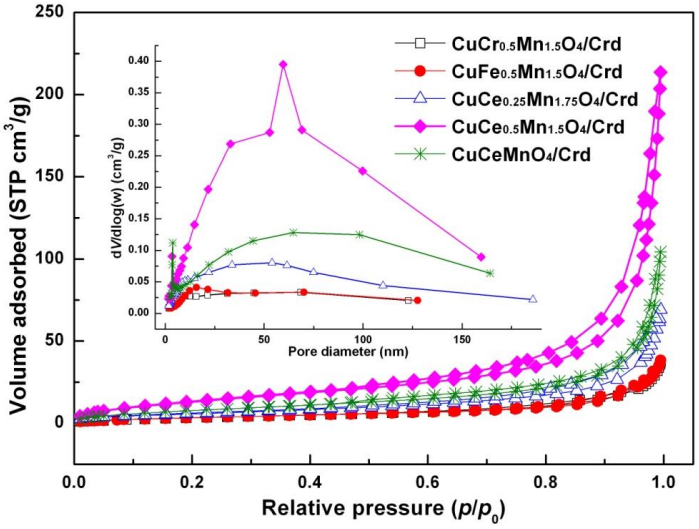
CuCr0.5Mn1.5O4/Crd
CuFe0.5Mn1.5O4/Crd
CuCe0.25Mn1.75O4/Crd
CuCe0.5Mn1.5O4/Crd
CuCeMnO4/Crd
Volume adsorbed (STP cm3/g)
Relative pressure (p/p0)
dV/dlog(w) (cm3/g)
Pore diameter (nm)

Fig. 3

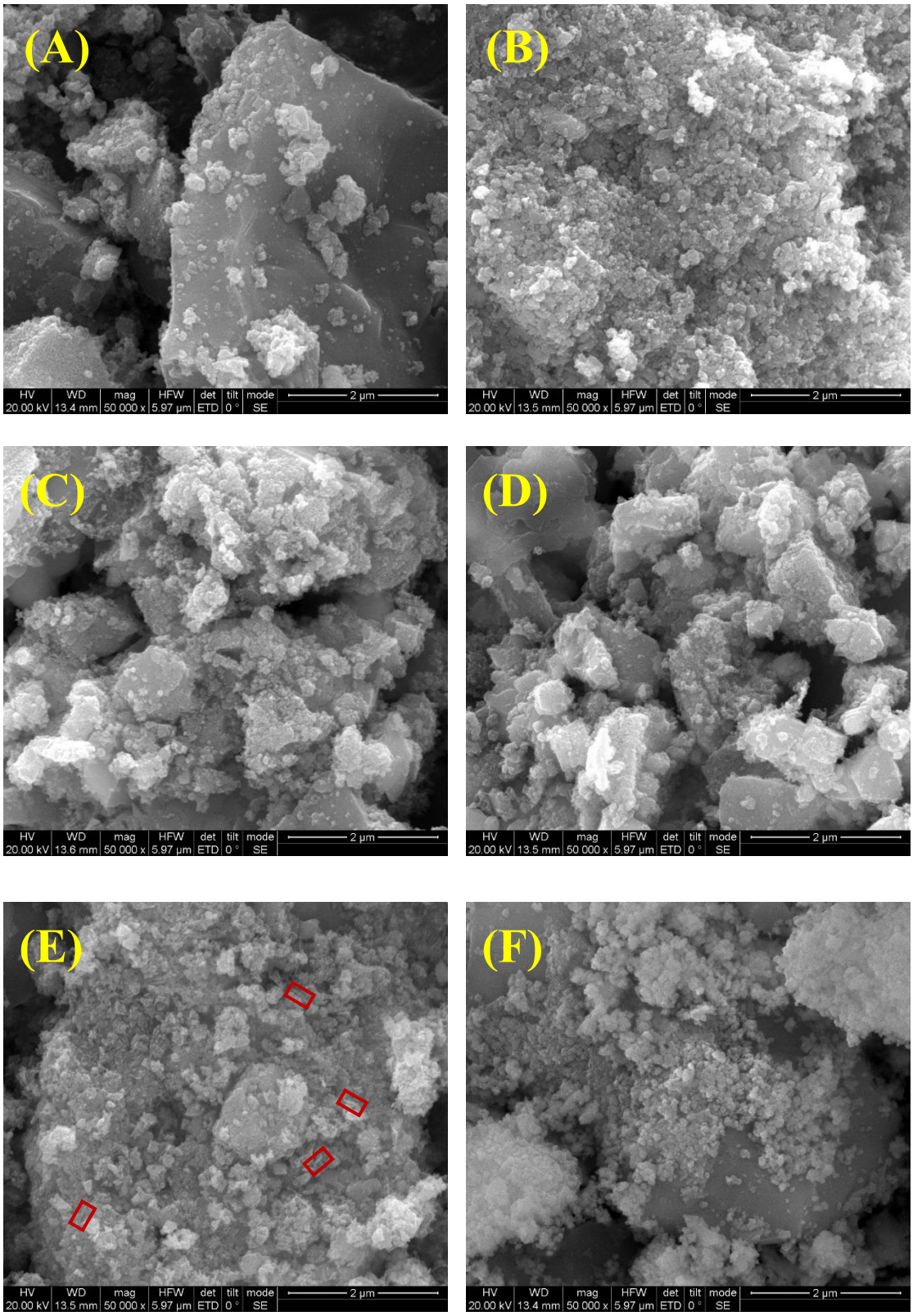
(A)
HV 20.00 kV | WD 13.4 mm | mag 50 000 x | HFW 5.97 µm | det ETD | tilt 0 ° | mode SE | 2 µm
(B)
HV 20.00 kV | WD 13.5 mm | mag 50 000 x | HFW 5.97 µm | det ETD | tilt 0 ° | mode SE | 2 µm
(C)
HV 20.00 kV | WD 13.6 mm | mag 50 000 x | HFW 5.97 µm | det ETD | tilt 0 ° | mode SE | 2 µm
(D)
HV 20.00 kV | WD 13.5 mm | mag 50 000 x | HFW 5.97 µm | det ETD | tilt 0 ° | mode SE | 2 µm
(E)
HV 20.00 kV | WD 13.5 mm | mag 50 000 x | HFW 5.97 µm | det ETD | tilt 0 ° | mode SE | 2 µm
(F)
HV 20.00 kV | WD 13.4 mm | mag 50 000 x | HFW 5.97 µm | det ETD | tilt 0 ° | mode SE | 2 µm

Fig. 4

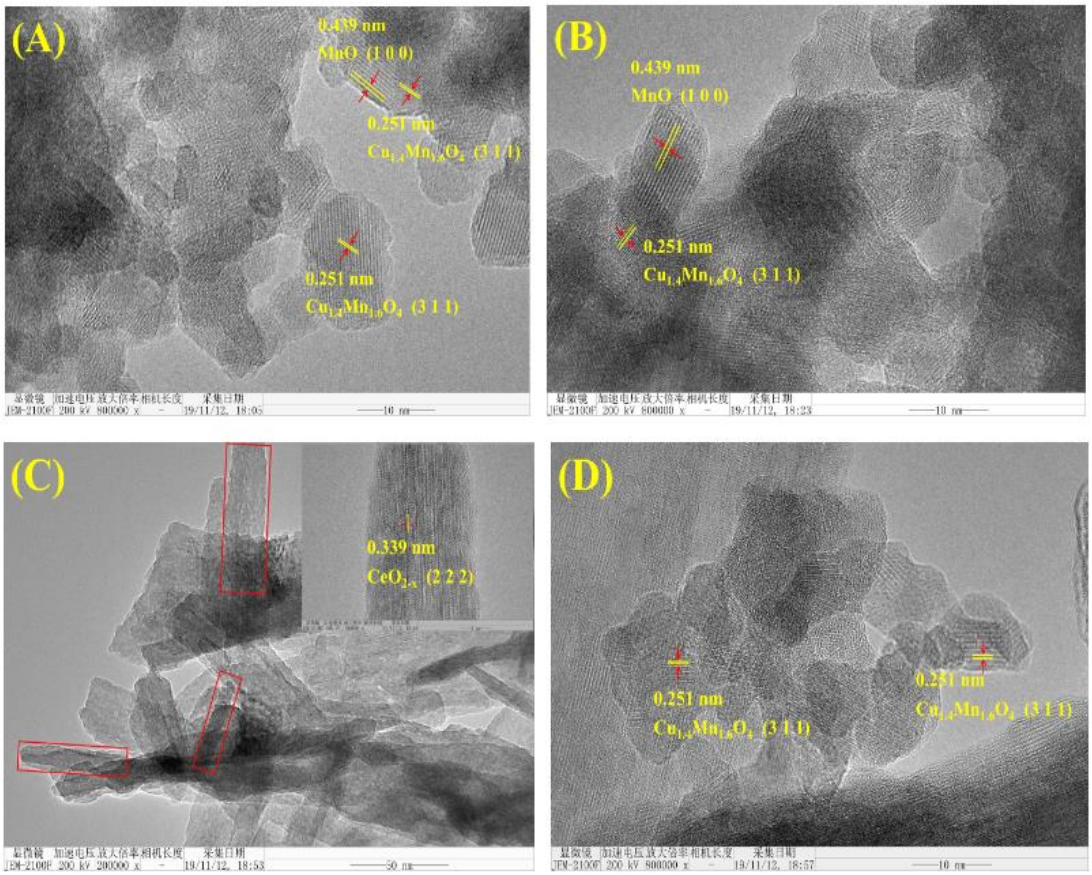
(A)
0.439 nm
MnO (1 0 0)
0.251 nm
$Cu_{1.4}Mn_{1.6}O_4$ (3 1 1)
0.251 nm
$Cu_{1.4}Mn_{1.6}O_4$ (3 1 1)
(B)
0.439 nm
MnO (1 0 0)
0.251 nm
$Cu_{1.4}Mn_{1.6}O_4$ (3 1 1)
(C)
0.339 nm
CeO_{2-x} (2 2 2)
(D)
0.251 nm
$Cu_{1.4}Mn_{1.6}O_4$ (3 1 1)
0.251 nm
$Cu_{1.4}Mn_{1.6}O_4$ (3 1 1)

Fig. 5

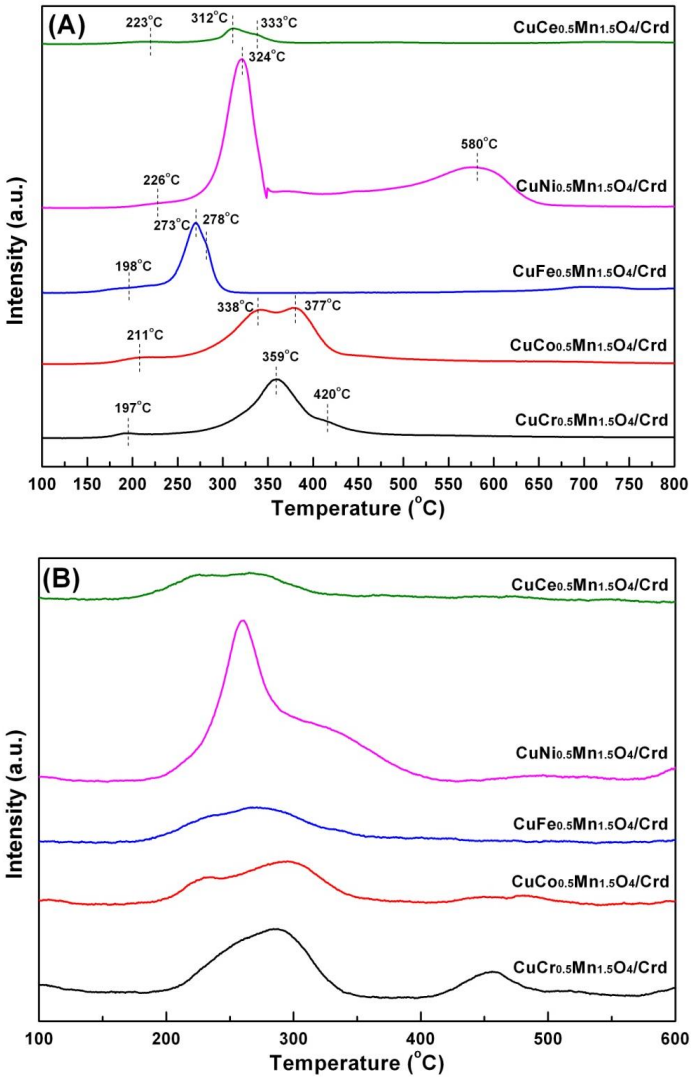
(A)
223°C
312°C
333°C
324°C
580°C
226°C
273°C
278°C
198°C
338°C
377°C
211°C
359°C
420°C
197°C
CuCe0.5Mn1.5O4/Crd
CuNi0.5Mn1.5O4/Crd
CuFe0.5Mn1.5O4/Crd
CuCo0.5Mn1.5O4/Crd
CuCr0.5Mn1.5O4/Crd
Intensity (a.u.)
100 150 200 250 300 350 400 450 500 550 600 650 700 750 800
Temperature (°C)
(B)
CuCe0.5Mn1.5O4/Crd
CuNi0.5Mn1.5O4/Crd
CuFe0.5Mn1.5O4/Crd
CuCo0.5Mn1.5O4/Crd
CuCr0.5Mn1.5O4/Crd
Intensity (a.u.)
100 200 300 400 500 600
Temperature (°C)

Fig. 6

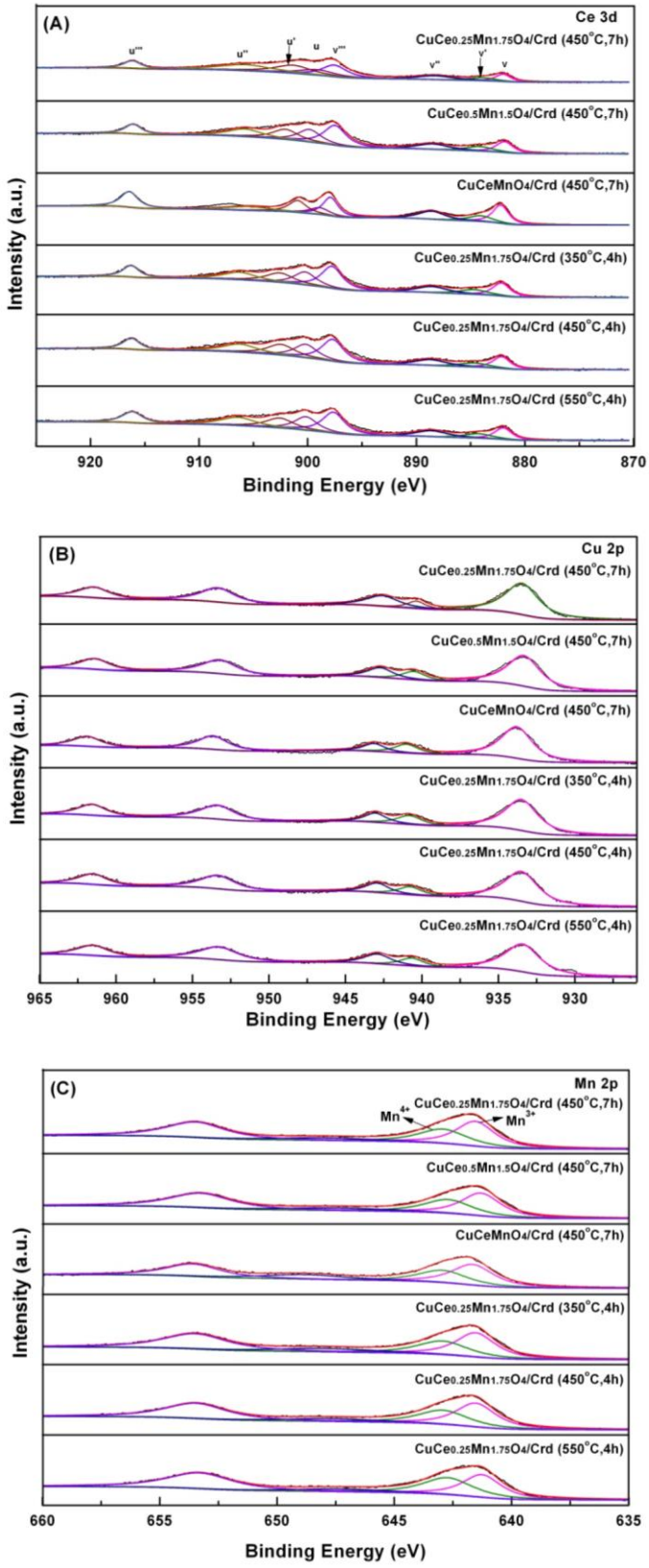
(A)
Ce 3d
CuCe0.25Mn1.75O4/Crd (450°C,7h)
CuCe0.5Mn1.5O4/Crd (450°C,7h)
CuCeMnO4/Crd (450°C,7h)
CuCe0.25Mn1.75O4/Crd (350°C,4h)
CuCe0.25Mn1.75O4/Crd (450°C,4h)
CuCe0.25Mn1.75O4/Crd (550°C,4h)
Intensity (a.u.)
920
910
900
890
880
870
Binding Energy (eV)
(B)
Cu 2p
CuCe0.25Mn1.75O4/Crd (450°C,7h)
CuCe0.5Mn1.5O4/Crd (450°C,7h)
CuCeMnO4/Crd (450°C,7h)
CuCe0.25Mn1.75O4/Crd (350°C,4h)
CuCe0.25Mn1.75O4/Crd (450°C,4h)
CuCe0.25Mn1.75O4/Crd (550°C,4h)
Intensity (a.u.)
965
960
955
950
945
940
935
930
Binding Energy (eV)
(C)
Mn 2p
Mn4+
Mn3+
CuCe0.25Mn1.75O4/Crd (450°C,7h)
CuCe0.5Mn1.5O4/Crd (450°C,7h)
CuCeMnO4/Crd (450°C,7h)
CuCe0.25Mn1.75O4/Crd (350°C,4h)
CuCe0.25Mn1.75O4/Crd (450°C,4h)
CuCe0.25Mn1.75O4/Crd (550°C,4h)
Intensity (a.u.)
660
655
650
645
640
635
Binding Energy (eV)

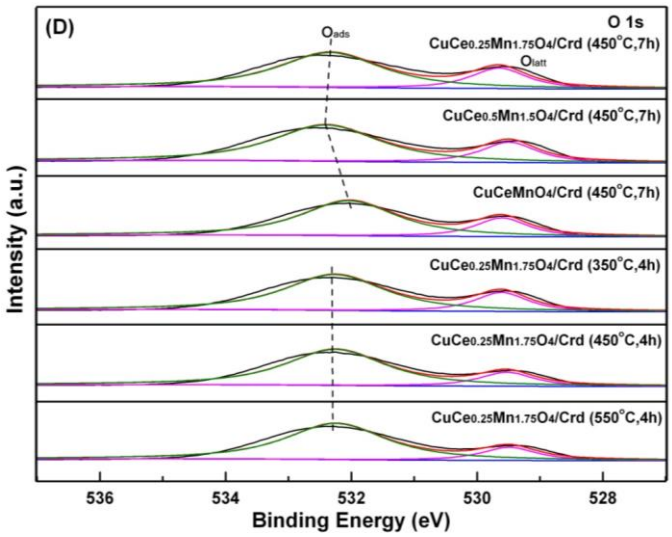
(D)
O 1s
O_{ads}
O_{latt}
$CuCe_{0.25}Mn_{1.75}O_4$/Crd (450°C,7h)
$CuCe_{0.5}Mn_{1.5}O_4$/Crd (450°C,7h)
$CuCeMnO_4$/Crd (450°C,7h)
$CuCe_{0.25}Mn_{1.75}O_4$/Crd (350°C,4h)
$CuCe_{0.25}Mn_{1.75}O_4$/Crd (450°C,4h)
$CuCe_{0.25}Mn_{1.75}O_4$/Crd (550°C,4h)
Intensity (a.u.)
536
534
532
530
528
Binding Energy (eV)

Fig. 7

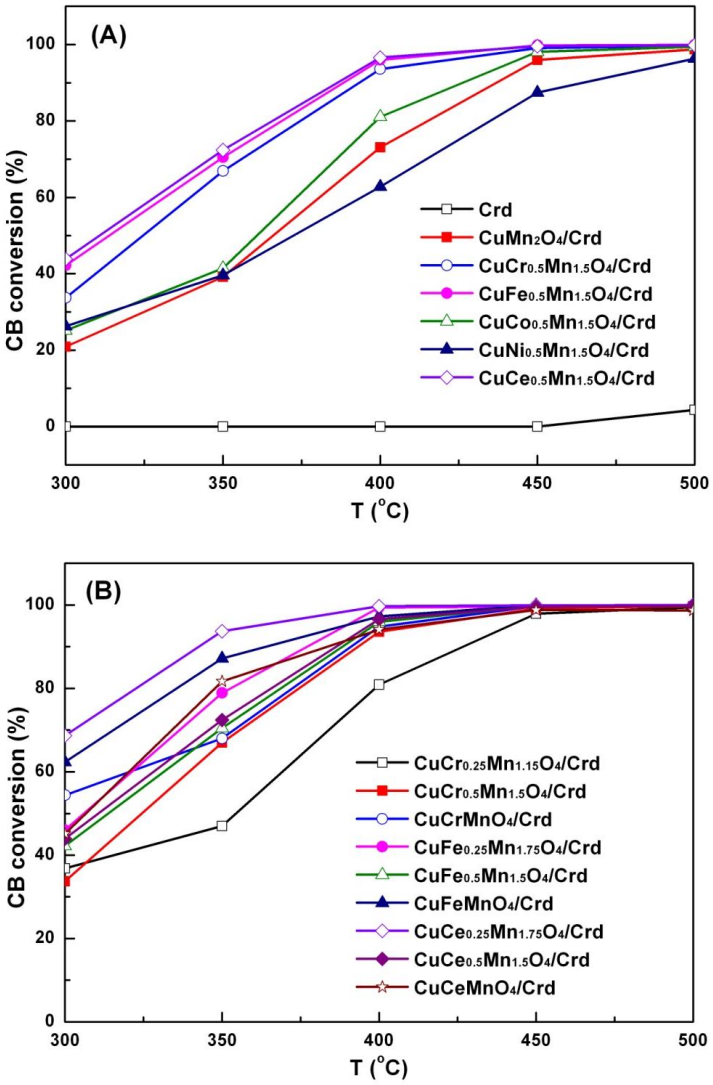
(A)
CB conversion (%)
T (°C)
Crd
CuMn2O4/Crd
CuCr0.5Mn1.5O4/Crd
CuFe0.5Mn1.5O4/Crd
CuCo0.5Mn1.5O4/Crd
CuNi0.5Mn1.5O4/Crd
CuCe0.5Mn1.5O4/Crd
(B)
CB conversion (%)
T (°C)
CuCr0.25Mn1.15O4/Crd
CuCr0.5Mn1.5O4/Crd
CuCrMnO4/Crd
CuFe0.25Mn1.75O4/Crd
CuFe0.5Mn1.5O4/Crd
CuFeMnO4/Crd
CuCe0.25Mn1.75O4/Crd
CuCe0.5Mn1.5O4/Crd
CuCeMnO4/Crd

Fig. 8

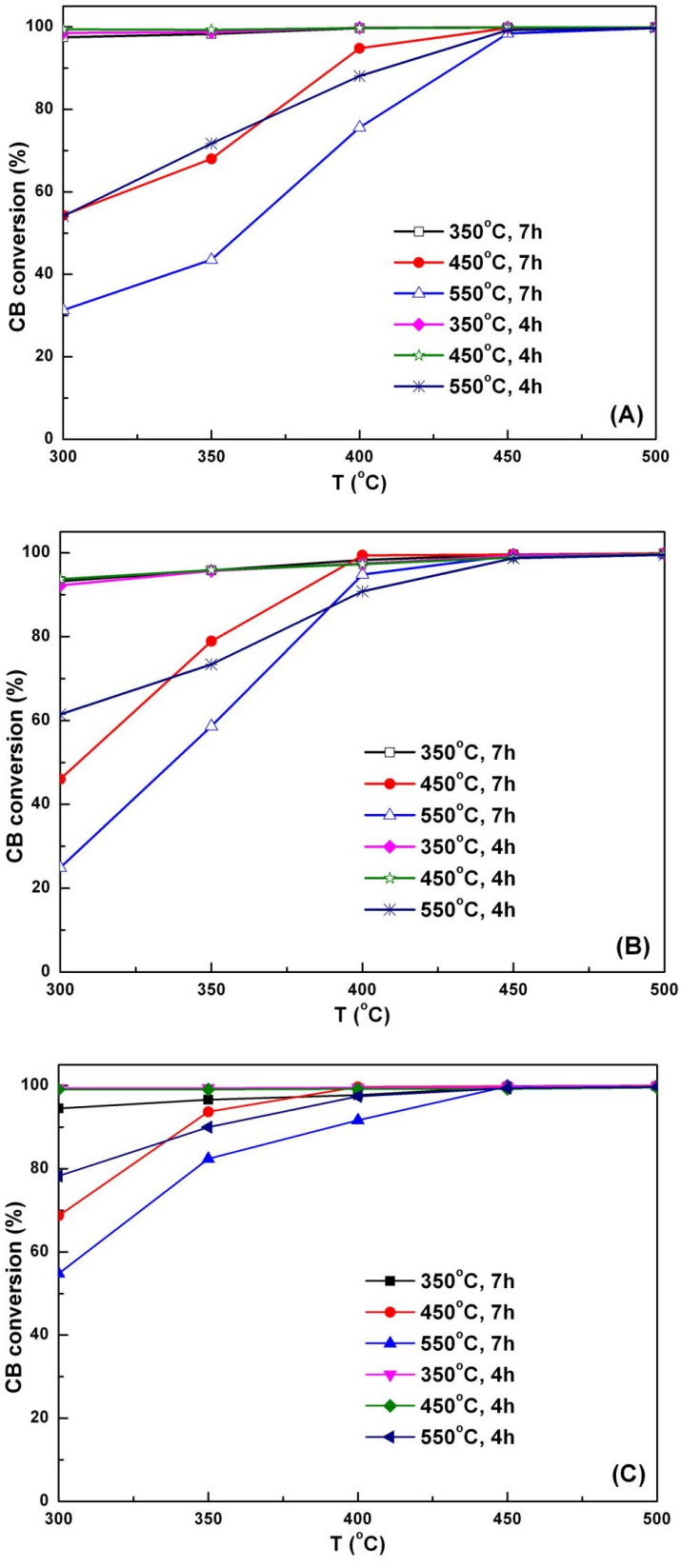
CB conversion (%)
T (°C)
350°C, 7h
450°C, 7h
550°C, 7h
350°C, 4h
450°C, 4h
550°C, 4h
(A)
(B)
(C)

Fig.9

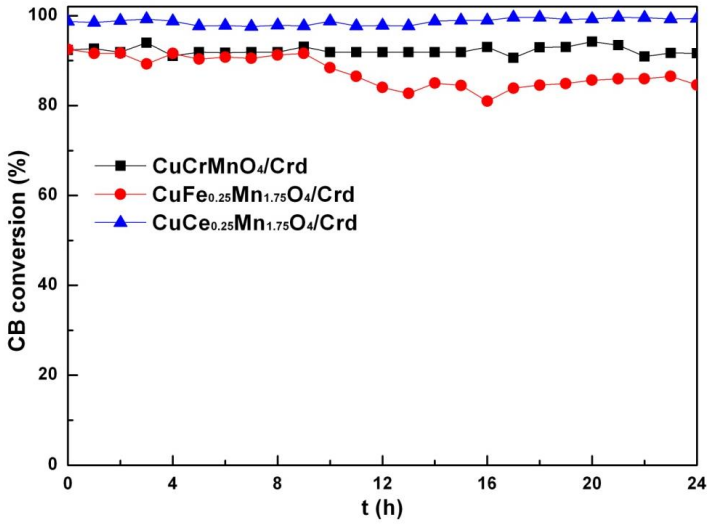
CB conversion (%)
t (h)
CuCrMnO4/Crd
CuFe0.25Mn1.75O4/Crd
CuCe0.25Mn1.75O4/Crd
0
20
40
60
80
100
0
4
8
12
16
20
24

Fig. 10

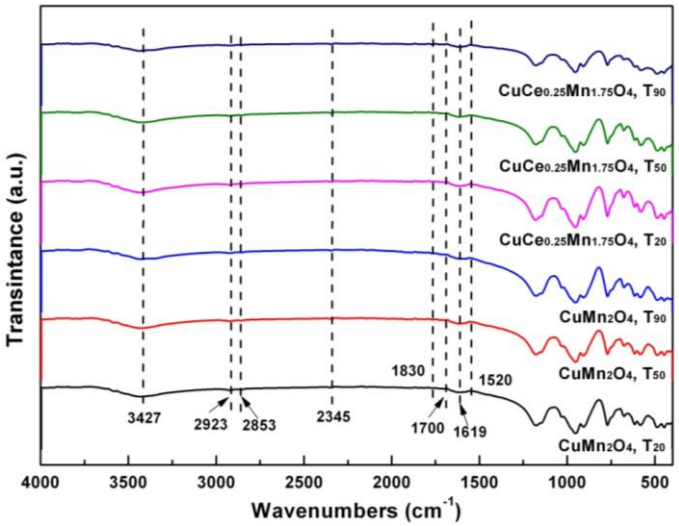
Transintance (a.u.)
Wavenumbers (cm-1)
4000
3500
3000
2500
2000
1500
1000
500
CuCe0.25Mn1.75O4, T90
CuCe0.25Mn1.75O4, T50
CuCe0.25Mn1.75O4, T20
CuMn2O4, T90
CuMn2O4, T50
CuMn2O4, T20
3427
2923
2853
2345
1830
1700
1619
1520

Fig. 11

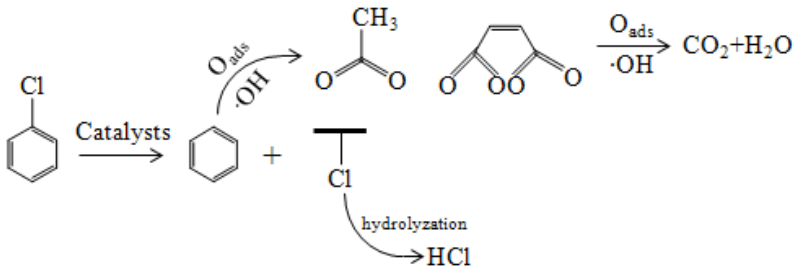
Cl
Catalysts
O_{ads}
·OH
CH_3
O
O
+
Cl
hydrolyzation
HCl
O
O
O
O
O_{ads}
·OH
CO_2+H_2O